A novel constitutive model for multi-step stress relaxation ageing of a pre-strained 7xxx series alloy

Jing-Hua Zheng [a]*, Jianguo Lin [a], Junyi Lee [a], Ran Pan [a], Chen Li [b], Catrin M. Davies [a,]

[a] Department of Mechanical Engineering, Imperial College London, London SW7 2AZ, UK

[b] The First Aircraft Institute, Xi'an, P. R. China

Abstract

A novel set of unified constitutive equations has been developed and validated to describe stress relaxation ageing (SRA) behaviour. The model, based on dynamic ageing and power-law creep relations, can predict the stress relaxation, age hardening response and their interactions at different temperatures, through considering the microstructure evolutions (precipitate radius, volume fraction and dislocation density) during SRA. In addition, the model newly incorporates the effects of prior cold work. This model was verified through T74 multi-step SRA experiments for different pre-strain conditions. Excellent agreement was achieved between the predicted and experimental stress relaxation and yield strength evolutions. The evolutions of micro-internal variables (e.g. normalised precipitate radius) within the model were calibrated by both the TEM results in this work and the experimental results from the literature. The model provides a valuable tool to predict the mechanical properties, and residual stresses post ageing, thus provides important guidance for designing manufacturing processes, leading to many benefits including reduced scrap rates and financial losses.

1   Introduction

Good mechanical properties in 7xxx series age-hardening aluminium alloys can be achieved by employing appropriate heat treatment processes, making it a popular material for load bearing components, especially for fabricating extra-large aircraft components (Heinz et al., 2000). These components are commonly produced by a forming process involving hot rolling/forging, solution heat treatment, quenching, cold-working and ageing (Zheng et al., 2018). Quenching, however, induces residual stresses (RS) in components, which lead to distortion issues. Residual stresses are relieved in the latter stages of the forming process (i.e. cold working and ageing) (Pan et al., 2016; Robinson et al., 2012). However, the complex geometries of the formed parts will result in complex stress states, which makes it difficult to eliminate RS completely and the remaining RS would cause component distortion after machine finishing (Robinson et al., 2012). Residual stress also impacts the precipitate evolution during ageing (Zheng et al., 2018) and may result in unacceptable mechanical performance in addition to structural integrity issues. To obtain satisfactory mechanical properties and further maximise the RS reduction, ageing is an important final step before post-processing, and a thorough understanding of the precise process is required. It should be noted that ageing is also the final opportunity to reduce any residual stresses. However, the interactive effects between residual stress relaxation and precipitate evolution during ageing are not well understood, and there are no appropriate models to describe these phenomena. To improve the manufacturing process in industrial applications and prevent issues caused by residual stresses, a fundamental understanding of the process and a prediction tool is required. Hence, in this work, an integrated stress relaxation ageing (SRA) model is developed to simulate and predict the stress relaxation and age hardening response.

Static artificial ageing models that are solely used for predicting the age hardening responses have been well established. These models were built on atomic diffusion and mass balance theories to characterize the evolution of the precipitates in ageing. The earliest isothermal ageing model was proposed by Shercliff and Ashby (1990), and Kampmann and Wagner (1984). They divided precipitate evolution into nucleation, growth and coarsening stages, and considered precipitate radius, solute concentrations and their contributions to the material's strength. Further modifications were made by Deschamps and Brechet (1998), who re-divided the model into two stages (i.e. nucleation and growth; growth and coarsening) and enabled a smoother prediction of precipitate nucleation, growth, coarsening and dissolution. A critical precipitate radius, r_c^*, which can neither grow nor dissolve, was introduced as a function of the temperature and the solute concentration. Myhr et al. (2000, 2004) summarized the ageing model and applied it to non-isothermal conditions using a discretization method. Other ageing models have been developed, improved and applied to different materials (Esmaeili et al., 2003), different applications (Bardel et al., 2016) and different pre-deformation levels (Bardel et al., 2016). However, these models were all developed for traditional static ageing behaviour. Thus, they did not consider residual stress relaxation and its effects on the precipitate hardening responses.

An integrated dynamic ageing model that can capture the precipitation response, the concurrent stress relaxation behaviour and their interactions are required to describe the ageing behaviour in the presence of residual stresses and, in addition, to constitutively describe the stress-strain relations during ageing. Considerable efforts have been made to build rate-dependent constitutive models to describe stress-strain responses (Yoshida, 2000; Ahad et al., 2014; Kabirian et al., 2014; Adzima et al., 2017; Shi et al., 2017) and stress relaxation behaviour (Krempl, 2001; Wang et al., 2004), some of which also introduced dislocation effects (Bertin et al., 2013; Khan and Liu, 2016; Yan et al., 2016) to their models. However, these models cannot describe the dynamic ageing behaviour. Existing creep-ageing models that describe similar dynamic coupling behaviour (between creep and precipitate hardening), provide a suitable foundation to develop an

SRA model. An early model used to predict the creep behaviour of AA7010 under a dynamic ageing condition was proposed by Ho et al., (2004). It introduced a simple relationship between creep and ageing by considering the hardening and softening effects. Lin et al., (2006) advanced the creep-ageing equations and enabled an integrated prediction of both precipitation hardening and creep. The effects of precipitate growth and the dislocation hardening were dynamically formulated into the creep formulation. Further improvements were made to describe the precipitation hardening behaviour of 7055 in creep-ageing by Zhan et al. (2011), where the evolution of normalised precipitate radius was used to describe both the precipitation hardening and the solute softening effects on the creep behaviour. Later, extensive work, including improving the creep-age models, such as accounting the precipitate aspect ratio (Zhang et al., 2015), considering the precipitate dissolution (Li et al., 2017) were performed. Studies have also been made to apply creep-ageing models to study different materials, such as AA6111 (Wang et al., 2004), AA2025 (Gu and Ngan, 2014), and study different conditions, such as T4, T651 (Lam et al., 2015), etc. An alternative approach based on a θ-projection method for modelling the creep-ageing behaviour, especially for 2024-T3 Al alloys, were also introduced by Lin et al. (2013). Though these existing models have been able to successfully predict the creep ageing behaviour, they are limited to cases where the dominating creep mechanism did not change, and the temperature and load remained constant. However, in many situations, the stress relaxation occurs within the material due to creep strain accumulation and, as seen in the Ashby deformation map (Frost and Ashby, 1973), the dominating creep mechanism may change with stress. These existing models did not consider the change in the dominating creep mechanism and are unable to describe the material behaviour accurately in these cases, for example stress relaxation. Additionally, these models, and their corresponding material parameters, can only model the creep-ageing behaviour for a specific material (e.g. 2050, 7055, etc.) under a single condition (e.g. T4, T6 etc.) at a specific temperature. However, the temperature is a key variable as it can significantly affect the rearrangement of the atoms, the stress relaxation process and the evolution of the microstructure (i.e. nucleation and growth of the precipitates). More importantly, most of the existing models mainly focused on predicting the creep deformation behaviour during the creep ageing process. The equations that described the corresponding hardening performance are limited in these models. The theoretical aspects, especially the effects of creep on the precipitate growth, are not treated rigorously in these models. Therefore, a comprehensive model that can fully describe the stress relaxation and the concurrent ageing behaviour is essential for modern manufacturing process, especially under multiple temperature conditions (i.e. T74 ageing treatment) and post different cold work magnitudes. These issues have been addressed in this work to derive a more rigorous constitutive model.

In this work, a set of unified constitutive equations, based on the dominating stress relaxation ageing mechanism, have been developed to predict the stress relaxation and the dynamic ageing responses under multiple temperature conditions and after different levels of cold work. The derivation of each equation, based on the static ageing models and the power-law creep model, has been presented in detail. These equations model both phenomena (ageing and stress relaxation) by introducing three micro-internal variables, (i.e. normalised precipitate radius, $\bar{r}$, volume fraction, $\bar{f}$, and normalised dislocation density, $\bar{\rho}$) and by considering their interactions. The equations were first verified by an experimentally observed multi-step stress relaxation ageing behaviour with different initial stresses (Zheng et al., 2018). To aid the micro-internal variable calibration in this model, both the TEM results, and the values of precipitate radius and volume fraction under similar pure ageing conditions (Dumont et al., 2003; Han et al., 2011; Liu et al., 2014; Sha and Cerezo, 2004; Stiller et al., 1999; Werenskiold et al., 2000; Zang et al., 2012) were employed. These equations were further applied to the multi-step stress relaxation ageing behaviour after different pre-strain levels. Comparisons between the predicted and experimental curves have been discussed in detail.

2   Physical-based constitutive model development

2.1   Microstructure evolution during stress relaxation ageing (SRA)

Traditional static ageing treatments harden the alloy by providing appropriate activation energy to the quench induced super saturate solid solution (SSSS), enabling a precipitate phase evolution: SSSS → GP zones → η' → η. This evolution and the precipitate distributions affect the material properties, including material strength and ductility. The peak strength of the material is achieved when the majority of the precipitates are finely distributed η' (Stiller et al., 1999). There are two major factors for achieving the peak strength when neglecting the complex grain structures inside the alloy. The first factor is the precipitate size: η' is similar to the critical precipitate in size, r_c, which can provide the highest cutting strength and in addition avoid dislocation bowing phenomenon (Shercliff and Ashby, 1990). The second factor is the volume fraction: a larger precipitate volume fraction is presented when the major phase of the precipitates is η' (Stiller et al., 1999) and this leads to more obstacles hindering the dislocation motion. Therefore, the precipitate size and volume fraction are selected as the two micro-internal variables that describe the age hardening responses.

Before the stress relaxation ageing (SRA) process, dislocations can be generated by prior cold work. During SRA the dislocation density will evolve, and may increase or decrease in value depending on the balance between creep strain generation, resulted from the stress relaxation, and dislocation recovery. The presence and evolution of dislocations alter the precipitates by creating more nucleation sites, leading to a faster nucleation, growth and coarsening phenomenon (Deschamps and Brechet, 1998). Therefore, a third micro-variable, dislocation density, is introduced to characterize its effects on the precipitate evolution (i.e. size and volume fraction evolution) and further on the age hardening responses. In turn, these dislocation–impacted precipitate characteristics also affect the creep resistance dynamically, thus further impacting the stress relaxation magnitude and the dislocation generations.

The mutual effects of prior cold-work, precipitate evolution (during ageing) and creep generation (during stress relaxation) under ageing temperatures on the SRA behaviour can be described as interactions between the precipitates and dislocations. Therefore, three major micro-features (i.e. precipitate size, volume fraction and dislocation density), their evolutions, interactions and their effects on creep and ageing response are included in the physical-based model described below.

2.2   Development of stress relaxation ageing (SRA) constitutive equations

Based on the description of the microstructure evolution above, a model has been developed, which enables the determination of the yield strength, σ_y, and the stress relaxation at different temperatures. The model is built using an internal state variable approach (Esmaeili et al., 2003; Li et al., 2017; Myhr and Grong, 2000), which relates the micro-internal variables to the material response of interest (i.e. yield strength, σ_y, creep strain, ε_c, etc.). The model consists of the following parts:

(a) Microstructure models, which predict precipitate size (r), volume fraction (f) and dislocation density (ρ) evolution during SRA. All these micro-internal variables are normalised by their critical values and will be described in detail below.

(b) Strength model (σ_y), which enables a prediction of the material strength in response to the relevant microstructural variables. The yield strength of the material is determined from three individual strengths i.e. precipitation strength: $\sigma_{ppt} = g_1(r, f, \rho)$; solute strength: $\sigma_{solute} = g_2(f)$; and dislocation strength: $\sigma_{dis} = g_3(\rho)$.

(c) Stress relaxation model (σ), which calculates the stress reduction due to the creep generation under dynamic ageing conditions. The model is based on the traditional power-law creep equation, with additional considerations from precipitate and dislocation effects.

2.2.1 Microstructure model

To simplify the model and facilitate its uptake by industry, instead of directly considering the evolution of each microstructural factors (r, f, ρ), the evolution of their normalised values (normalised precipitate radius, $\bar{r}$, normalised volume fraction, $\bar{f}$, and normalised dislocation density, $\bar{\rho}$), are used in the model. These normalised internal variables are representative of the overall behaviour of the material during SRA, thus providing an accurate trend on the material response of interests.

2.2.1.1 Normalised precipitate radius ($\bar{r}$)

Precipitate evolution is a complex process where nucleation, growth, coarsening and dissolution occurs simultaneously. A precipitate can either grow or dissolve depending on the current temperature, current and equilibrium solute concentrations (Myhr and Grong, 2000). To quantitatively characterize the size evolution, Kampmann and Wagner (1984), and Shercliff and Ashby (1990) introduced the first two sets of equations based on diffusion theories. The models were further developed by Myhr et al. (2000, 2004) and Deschamp et al. (1998) to enable predictions for different heat treatable alloys under different ageing conditions. Table 1 lists the equations used for simulating precipitate growth, where r is the average precipitate radius and t is the ageing time.

Table 1 Equations to describe precipitate growth in various models

Models	Radius equations from the model	Description
Kampmann and Wagner (1984); Myhr, et al. (2000, 2004)	$$\dot{r} = \frac{dr}{dt} = \frac{\bar{c} - c_i}{c_p - c_i} \frac{D}{r}$$	$\bar{c}$: mean concentration c_i : interfacial concentration c_p: precipitate concentration D: diffusion coefficient
Shercliff and Ashby (1990)	$$r^3(t) - r_0{}^3 = \frac{c_1 t}{T} exp(\frac{-Q_A}{RT})$$	r_0: The precipitate radius at t=0 c_1 : kinetic variable t: ageing time T : ageing temperature in Kelvin Q_A: diffusion activation energy R : Universal gas constant
Deschamps et al. (1998); Nicolas and Deschamps (2003)	$$\dot{r} = \frac{D}{r}\left[\frac{C - C_{eq}\exp\left(\frac{R_0}{r}\right)}{1 - C_{eq}\exp\left(\frac{R_0}{r}\right)}\right]$$	D : diffusion coefficient C : solute concentration C_{eq}: equilibrium concentration R_0: temperature dependent variable

From a detailed examination of the previous equations in Table 1, a general expression for precipitate growth can be summarised as:

$$\dot{r} = \frac{D_{eff_1}}{r^n} \tag{1}$$

where D_{eff_1} is considered as the effective diffusion coefficient.

A normalised radius, $\bar{r}$, is introduced

5

$$\bar{r} = \frac{r}{r_c} \tag{2}$$

where r_c is the average precipitate radius under the peak aged state, usually around 5 nm (Werenskiold et al., 2000) for 7xxx series aluminium alloy. Note that ageing is expected to reach its peak when the normalised average radius achieves unity. An under-aged state and over-aged state can be described when $\bar{r} < 1$ and $\bar{r} > 1$, respectively. Substituting the normalised average radius into Eqn. (1), gives

$$\dot{\bar{r}} = \frac{D_{eff_1}/r_c^{n+1}}{\bar{r}^n} = \frac{D_{eff_2}}{\bar{r}^n} \tag{3}$$

This general form is suitable for characterizing precipitate growth. However, it has difficulty modelling the early stage of ageing, where the precipitate size is infinitesimally small ($r \approx 0$). A different form, Eqn. (4), is then adopted to enable a similar radius evolution with r starting from 0, as suggested in (Li et al., 2017),

$$\dot{\bar{r}} = D_{eff}(\bar{R}_{max} - \bar{r})^{m_{r_1}} \tag{4}$$

where D_{eff} is the effective diffusion coefficient and m_{r_1} is a material constant. When $r = \bar{R}_{max}$ then $\dot{\bar{r}} = 0$. Thus, $\bar{R}_{max}$ is considered as the maximum normalised average precipitate size that could be formed at a specific temperature. This parameter is introduced based on experimental results in (Werenskiold et al., 2000), where the average precipitate size reaches a certain value, depending on the ageing temperature, and precipitate growth rate reduces to ~0 when ageing time exceeded 24 hrs. The value of $\bar{R}_{max}$ depends on the temperature and is expressed in the form of the Arrhenius law as shown in Eqn. (5).

$$\bar{R}_{max} = \bar{R}_{max_0} \cdot \exp\left(-\frac{Q_v}{RT}\right) \tag{5}$$

In Eqn. (5), Q_v is the bulk diffusion activation energy, $\bar{R}_{max_0}$ is a material constant, R is the universal gas constants, T is the SRA temperature in Kelvin. Two assumptions were adopted: (1) precipitates were considered as spherical in the process of SRA; (2) the influences of the dislocation core diffusion on $\bar{R}_{max}$ were ignored.

In terms of D_{eff}, the earliest expression (Poole, 1997) is defined as in Eqn. (6), which consists of two parts: the contribution from bulk diffusion, $f_v D_v$, and the contribution from dislocation core diffusion, $f_c D_c$.

$$D_{eff} = f_v D_v + f_c D_c = D_{v_0} exp\left(-\frac{Q_v}{RT}\right) + \gamma_c \rho \cdot D_{c_0} exp\left(-\frac{Q_c}{RT}\right) \tag{6}$$

where f_v, f_c, D_v, D_c are the atomic fractions and diffusivities in the bulk matrix and in the dislocation core, respectively. As reported in (Robinson and Sherby, 1969), f_v is taken to be unity. D_v is a function of the bulk diffusion activation energy, Q_v, and a material parameter, D_{v_0}. f_c is suggested to be proportional to the dislocation density, ρ, and the effective dislocation core cross-sectional area, γ_c (Poole, 1997). Similar to D_v, D_c is also expressed in Arrhenius form, where Q_C denotes the dislocation core diffusion activation energy, D_{c_0} is a material parameter. This equation is well established, especially for FCC pure metals (Balluffi, 1970). However, it cannot adequately describe SRA behaviour, where precipitates and dislocations change dynamically.

To enable precipitate evolution characterisation, an advanced expression for D_{eff} is introduced as follows.

$$D_{eff} = A_r \left\{ exp\left(-\frac{Q_v}{RT}\right) + a_c[1 - exp(-\alpha_1 \bar{r})]exp\left(-\frac{Q_c}{RT}\right) \bar{\rho}^{m_r} \right\} \tag{7}$$

6

where A_r is a coefficient used to quantify the magnitude of D_{eff}. a_c is a calibrated constant related to γ_c, D_{c_0} and D_{v_0} in Eqn. (6). α_1 and m_r determine the weight of the dislocation core diffusion. Compared with Eqn. (6), three improvements were made in the definition of D_{eff} in Eqn. (7). Firstly, the term $[1 - exp(-\alpha_1 \bar{r})]$ has been introduced, to quantify the influence of dislocation core diffusion, which varies with the evolution of the precipitate radius inside the bulk matrix. When an alloy undergoes a transformation from SSSS to the peak-aged state, the aluminium matrix contains an extremely large quantity of small bulk precipitates. The bulk diffusion dominates the precipitation process compared to dislocation core diffusion. The magnitude of this term is relatively small. When the alloy transforms from its peak-aged to over-aged state, then dislocation core diffusion becomes increasingly important compared to the bulk diffusion, where larger and less bulk precipitates are formed. The magnitude of this term increases with $\bar{r}$. Secondly, the effects of dislocation density on the dislocation core diffusivity, D_c, is considered, such that $D_c \propto \rho^{m_r-1}$. It was reported in (Balluffi, 1970) that D_c may be affected by the current dislocation density, though previous modelling work assumed that D_c was independent of ρ, such as in (Poole, 1997). Knowing that $f_c \propto \rho$, gives $f_c D_c \propto \rho^{m_r}$. Thirdly, in contrast to Eqn. (6), where the absolute dislocation density magnitude was used, a normalised dislocation density, $\bar{\rho}$, was adopted in Eqn.(7). Details on $\bar{\rho}$ is described in Section 2.2.1.3.

There are several advantages of using Eqns. (4), (5), (7). Firstly, the equations give an appropriate mechanism-based expression of the dynamic evolution of the precipitates within the grain. Secondly, the effects of the dislocation on the growth of the precipitates both in the bulk matrix and around dislocations are fully described by distinguishing the two diffusion patterns. Thirdly, temperature effects are considered using the form of Arrhenius law. Fourthly, the equations can give a continuous prediction of the precipitate radius evolution from nucleation to coarsening, thus simplifying the equations and making them more suitable for industrial application.

2.2.1.2 Normalised volume fraction ($\bar{f}$)

The earliest expression for the volume fraction, f, proposed by Shericliff and Ashiby, (1990), is shown in Eqn. (8).

$$f(t) = f_e \left[1 - exp\left(-\frac{t}{\tau}\right)\right] \tag{8}$$

where τ is the time constant, f_e is the equilibrium volume fraction and t is the ageing time.

Substituting a normalised volume fraction ($\bar{f} = f/f_e$) into Eqn. (8) and differentiating it with respect to time, gives

$$\dot{\bar{f}} = \frac{1}{\tau}(1 - \bar{f}) \tag{9}$$

Subsequent modelling work has been conducted to improve the volume fraction expression and to enable the equation to be used for different applications, e.g. under non-isothermal conditions (Myhr and Grong, 2000), for different series of alloys (Liu et al., 2003), etc. Myhr and Grong, (2000) considered the precipitate size distribution and calculated the volume fraction by integrating the precipitate size distribution. Liu et al. (2003) calculated the volume fraction directly from the precipitate radius ($\propto r^3$). Since the volume fraction is not only related to time (i.e. Eqn. (8)), but also related to the precipitate size, the normalised volume fraction can newly be described by

$$\dot{\bar{f}} = A_f \cdot (1 - \bar{f}) \cdot \dot{\bar{r}} \cdot \bar{r}^2 \tag{10}$$

where A_f is the pre-exponential constant, and the term $(1 - \bar{f})$ brings in the influence from a substantial increase in the quantity of precipitates at the early stage of ageing (Sha and Cerezo, 2004). This influence become less important with ageing time (value decreases from 1 to 0), thus this can reflect the rapidly decrease in the increase rate of the precipitate density. The term $\dot{\bar{r}} \cdot \bar{r}^2$ accounts for the effects of each precipitate's volume. When the material reaches its peak strength, $\bar{f}$ reaches its equilibrium value of 1 and $\dot{\bar{f}}$ remains at 0 and is subsequently unaffected by the continuous coarsened precipitates. AN assumption is made that all the elements, such as Zn, Mg, etc. elements are depleted after the material reaches its peak strength, and the precipitates then coarsen by competitive growth at a constant volume fraction (Shercliff and Ashby, 1990).

2.2.1.3   Normalised dislocation density ($\bar{\rho}$)

The third micro-scale internal variable is the normalised dislocation density, which has also been used as an input in Eqn. (7). The dislocation is normalised by the maximum dislocation density, which is expressed as follows,

$$\bar{\rho} = \frac{\rho}{\rho_m} \tag{11}$$

where ρ_m is the maximum dislocation density that can be formed in the material at 273 K. Thus, $\bar{\rho}$ varies from 0 to 1. The evolution of the normalised dislocation density, according to (Haddadi et al., 2006; Zhan et al., 2011), is described by Eqn. (12) and (13).

$$\dot{\bar{\rho}} = A_d(1 - \bar{\rho})|\dot{\varepsilon}_c| - C_d\bar{\rho}^{m_5} \tag{12}$$

$$C_d = C_{d_0} \cdot exp\left(-\frac{Q}{RT}\right) \tag{13}$$

For clarity, $\bar{\rho}$ is a simplified parameter that describes the global effects of all types of dislocations, including screw and edge dislocations. ε_c is the creep strain generated during SRA and is later expressed in Eqn.(27) and A_d, C_d, m_5 are material constants characterizing the dislocation generation (due to creep), dynamic and static recovery processes. Higher temperatures can facilitate the dislocation recovery process, especially for static recovery (Farla et al., 2011). Here, C_d is considered as a temperature dependent constant determining the extent of static recovery, and should satisfy Eqn. (13). An assumption that the dynamic recovery is almost unaffected by the changing temperature was made.

2.2.2   Strength model

The overall strength of the artificially aged material is attributed to precipitate strength, σ_{ppt}, solid solute strength, σ_{solute}, and dislocation strength, σ_{dis} , neglecting any grain size induced strengthening phenomena. Their contributions to the yield strength, σ_y, are as follows.

$$\sigma_y = \sigma_{solute} + \sqrt{\sigma_{ppt}^2 + \sigma_{dis}^2} \tag{14}$$

Here, a classical law of mixtures was adopted to including the precipitate and dislocation strengthening contributions (i.e. σ_{ppt} and σ_{dis}) to the overall yield strength (Kock et al., 1975). While the solute strength contribution was added linearly. This approach was adopted from many studies, including Deschamps and Brechet, (1998), Poole et al., (2000), Zhan et al., (2011) and Li et al., (2017), which described the contributions of 3 strengthening components to the final yield strength and obtained good agreement with experimental results. Therefore, Eqn. (14) is a semi-empirical equation with a slight modification from the

work by Kock et al., (1975). The values of different strength contributions are related to the microstructure variables, assuming that temperatures can only affect the strength by affecting the microstructure evolution ($\bar{r}, \bar{f}, \bar{\rho}$). Hence, the temperature dependent constants are introduced into the strength implicitly via the equations that describe the microstructure evolution ($\bar{r}, \bar{f}, \bar{\rho}$).

2.2.2.1 The contribution of precipitates to the strength (σ_{ppt})

The earliest models that described the precipitate strengthening response, contributed by shearable and non-shearable precipitates, were developed by Shercliff and Ashby, (1990) and Kampman and Wagner (1984), where it is postulated that shearable and non-shearable precipitates contributed to the precipitate strength. Shercliff and Ashby, (1990) described the precipitate strengthening response combining the precipitate shearing and by-passing mechanism, and calculating their harmonic mean values. Kampman and Wagner (1984) (KWN) proposed an alternative discrete approach, where the precipitate size distribution was considered. Myhr et al., (2001) further improved KWN model and enabled it to capture the coupled nucleation, growth and coarsening phenomena. The equations regarding the different approaches are given below.

Shercliff and Ashby, (1990), proposed the following equations

$$\sigma_{ppt} = \left(\frac{1}{\sigma_A} + \frac{1}{\sigma_B}\right)^{-1} \tag{15}$$

$$\sigma_A = c_3 f^{1/2} r^{1/2}; \qquad \sigma_B = c_4 f^{1/2} r^{-1} \tag{16}$$

Substituting Eqn. (16) into Eqn. (15) yields:

$$\sigma_{ppt} = \left(\frac{1}{\sigma_A} + \frac{1}{\sigma_B}\right)^{-1} = \left(\frac{1}{c_3 f^{1/2} r^{1/2}} + \frac{1}{c_4 f^{1/2} r^{-1}}\right)^{-1} = \left(\frac{1}{c_3 r^{0.5}} + \frac{r}{c_4}\right)^{-1} \cdot f^{0.5} = \sigma_r \cdot f^{0.5} \tag{17}$$

where σ_A, σ_B are strength contributions from shearable and non-shearable precipitates, c_3 and c_4 are material constants that are influenced by shear modules and the Burgers vector. r and f are the precipitate size and volume fraction, respectively.

Myhr et al., (2001) proposed an alternative formulation,

$$\sigma_{ppt} = \frac{MF}{bl} = \frac{M}{br}(4/3 \cdot \beta G b^2 \pi)^{-0.5} \bar{F}^{3/2} \cdot f^{0.5} = \sigma_r \cdot f^{0.5} \tag{18}$$

where M is the Taylor factor, b is the Burgers vector, r is the mean precipitate radius, G is the shear modulus, β is a material constant, $\bar{F}$ is the mean precipitate strength and determined by the precipitate radius.

By a detailed examination of Eqn. (17) and (18), one can conclude that σ_{ppt} is equal to the product of the radius contributed strength, σ_r, and volume fraction contributed strength, $f^{0.5}$. A further modification to the expression of σ_r (in its rate form) was made to derive Eqn.(19),

$$\dot{\sigma}_r = C_r \dot{\bar{r}}^{m_2}(1 - \bar{r}) \tag{19}$$

where C_r and m_2 are material constants.

In reality, the precipitates in the Al-matrix have a size distribution, while dislocations are hindered by a complex pattern of the precipitates. Therefore, this modification expresses the global effects of the average normalised precipitate size on the material strength, where the strength initially increases (i.e. under-age to

peak-age) followed by a decrease (peak-age to over-age) when the normalised precipitate radius continues increasing. In addition, Eqn. (19) is more appropriate to describe σ_r using the normalised precipitate radius, $\bar{r}$, where precipitate strength can be easily identified by the normalised precipitate radius, $\bar{r}$, for example the, material is under-aged when ($\dot{\sigma}_r > 0$; $\bar{r} < 1$), it is at peak-aged condition when ($\dot{\sigma}_r = 0$; $\bar{r} = 1$) and over-aged when ($\dot{\sigma}_r < 0$; $\bar{r} > 1$) (Zhan et al., 2011).

In Eqns (17) and (18), the volume fraction f was then replace by a normalised value, $\bar{f}$, to give

$$\sigma_{ppt} = \sigma_r \cdot \bar{f}^{m_1} \tag{20}$$

where m_1 is a material constant, and is suggested to be around 0.5 (Myhr et al., 2001, Barlat et al., 2002; Li et al., 2009).

2.2.2.2 The contribution of solid solutes to the strength (σ_{solute})

The strengthening contribution from the solid solution is controlled by the solute concentration, c. The basic relationship (Shercliff and Ashby, 1990; Deschamps and Brechet, 1998) between σ_{solute} and c is given in Eqn. (21),

$$\sigma_{solute} = C_{ss_0} \, c^{m_3} \tag{21}$$

where C_{ss_0} and m_3 are material constants. An analytic theory was developed by Leyson et al., (2010) to enable a parameter free prediction of the solute strenghen by establishing a relationship between the dislocation movement energy and the dislocation-solute interacation energy. This new theory improves the prediction of the solute strength. However, however, experienced an underestimation where Fe solutes were presented in the Al alloy. For commercial alluminium alloys, Fe is the most common impurity found in aluminium. Therefore, to enable the global solute strength for commercial aluminium alloy to be characterized, the relative simplifed form, Eqn. (21), was adopted in our study, where the solute strength evolution is expressed by the temperature dependent solute concentration.

Eqn. (22) introduces the relationship between $\bar{f}$ and c based on mass balance theories.

$$\bar{f} = \frac{f}{f_e} = \frac{c_i - c}{c_i - c_e} \tag{22}$$

where c_i and c_e are initial and equilibrium solute concentrations, which are constants depending on the chemical composition of the alloy. Substituting Eqn. (22) into Eqn. (21) yields a solute strength equation, which is a function of $\bar{f}$.

$$\sigma_{solute} = C_{ss0} \cdot c_i \left(1 - \frac{c_i - c_e}{c_i} \cdot \bar{f}\right)^{m3} = C_{ss}\left(1 - B_{ss}\bar{f}\right)^{m3} \tag{23}$$

where C_{ss} and B_{ss} are constants relating to initial and equilibrium solute concentrations.

For clarity, the temperature effects on the solid solute strengthen are considered from $\bar{f}$, i.e. Eqn. (10), which is a temperature dependent micro-internal variable. The material strength is a macroscopy reflection of the microstructure evolution. Therefore, an assumption has been made that temperature can only affect the material strength response by impacting the micro-internal variable.

2.2.2.3 The contribution of dislocations to the strength

The general dislocation hardening law (Zhan et al., 2011) is adopted here:

$$\sigma_{dis} = A_{ds} \, \overline{\rho}^{m_4} \tag{24}$$

A_{ds} a material constant that is related to the shear modulus, Burgers vector, etc. m_4 is a material constant, and was suggested to be around 0.5 (Taylor, 1934).

2.2.3 Stress relaxation model (σ)

Under displacement (or strain) controlled loading conditions, creep strain accumulation results in stress relaxation since the creep strain accumulation is accommodated by a reduction in the elastic strain. A significant change in stress may alter the dominant creep mechanisms, and thus an advanced model is required to fully describe the stress relaxation behaviour, which is described below.

The original power-law creep relationship, according to (Mukherjee et al., 1968; Kocks, 1976), to describe the climb-controlled creep behaviour is given in Eqn (25),

$$\dot{\varepsilon}_c = AD_v \left(\frac{\sigma}{\mu}\right)^n \tag{25}$$

where σ is the applied stress, μ is the shear modulus, n is the stress exponent, D_v is the bulk diffusion coefficient and A is a temperature dependent material constant. n is expected to be a constant, (e.g. $n = \sim3$ for some materials (Brown and Ashby, 1980)) when creep occurs at a constant temperature and stress. However, the value of n was found varies from 1–10 (Mukherjee et al., 1968; Somekawa et al., 2005) when a wider range of the stresses are applied. Therefore, during the stress relaxation process, the dominant creep mechanism and thus n may change with time. To enable the equation to capture the change in dominating creep mechanism, due to the decreasing stress, and give better predictions of the stress relaxation curves, a modification on the stress exponent n is necessary.

At the conventional ageing temperature (i.e. ~ 180 °C for 6xxx and ~ 120 °C +170 °C for 7xxx aluminium alloy), the Ashby deformation map (Frost and Ashby, 1973) suggests that the dominating creep mechanism may change when the applied stress decreases. The change in the creep mechanism is attributed to the effects of the dislocation core diffusion (Frost and Ashby, 1982). When the dislocation density varies, the effective activation volume may be affected, and thus a change in the stress exponent, n, may occur. In addition, the experimental results in (Zheng et al., 2018) also indicated that the pre-strain level ahead of the stress relaxation process affects the n value during subsequent stress relaxation. Therefore, the dislocation density is a main factor that can impact the dominating creep mechanism, and hence the stress exponent, n, varies with stress reduction. Based on the theory above and the experimental results (Zheng et al., 2018), an improved power-law equation, Eqn (26), was developed, where the normalised dislocation density is directly related to the stress exponent to account for the dislocation induced mechanism change.

$$\dot{\varepsilon}_c = A_s \left(\frac{\sigma}{\sigma_0}\right)^{n(1+\overline{\rho})} \tag{26}$$

In Eqn (26) A_s is a temperature dependent constant. During the stress relaxation ageing, dynamic ageing occurs simultaneously with creep deformation, and the evolution of the precipitates lead to a varied creep resistance. To account for the effects of dynamic ageing on creep strain evolution, Eqn. (26) can be modified, such that the creep resistance (i.e. kσ_y) is substracted from the applied stress, and hence

$$\dot{\varepsilon}_c = A_s \left(\frac{\sigma - k\sigma_y}{\sigma_0}\right)^{n(1+\overline{\rho})} \tag{27}$$

Note that the creep resistance is supposed to vary in the same way as yield strength, σ_y, since both depend on dislocation mobility, which is greatly impacted by the precipitate sizes and distributions. In addition, the established equation for yield strength (σ_y), Eqn. (14), in this work is the macro response of the precipitation process, which evolves with ageing time. Therefore, Eqn (27) includes the dynamic precipitation effects on the creep behaviour. Considering the interaction between the creep and precipitation process, the precipitate evolution impacts yield strength evolution (i.e. Eqn. (14)), and thus creep strain generation (i.e. Eqn.(27)). In turn, the creep generation affects the evolution of the normalised dislocation density (i.e. Eqn. (12)), and subsequently, the formation of precipitates (i.e. Eqn. (4)). The temperature dependent material parameter, k, determines the extent of the effects of precipitation on the concurrent creep strain generation. Here, σ_0 is a material constant (Wang et al., 2004), often taken to be unity. The temperature dependency of A_s and k are described by an Arrhenius law, as given in Eqn. (28) and (29),

$$A_s = A_{s_0} \cdot exp\left(-\frac{Q}{RT}\right) \tag{28}$$

$$k = k_0 \cdot exp\left(\frac{Q}{RT}\right) \tag{29}$$

where A_{s_0} and k_0 are constants and Q is creep activation energy.

2.2.4   Unified constitutive equations

An integrated SRA model can be derived by assembling the proposed micro-structural equations (i.e. Eqns. (4), (5), (7), (10), (12), (13)), strength equations (i.e. Eqns. (14), (19) ,(20), (23), (24)) and the stress relaxation equations (i.e. Eqns.(27), (28), (29)). Each equation is not only time and temperature dependent, but are also interdependent and thus affect the relevant SRA features, such that the creep strains (i.e. Eqn.(27)) generated during SRA lead to a change in the dislocation density (i.e. Eqn. (12)). This dislocation evolution affects the precipitate radius (i.e. Eqns. (4), (5), (7)), simultaneously leading to a dynamically changed age hardening response (i.e. Eqns. (14), (19), (20)). This age hardening response then affects the creep generation in SRA (i.e. Eqn. (27)).

3   Model implementation

The sets of constitutive equations were then applied to simulate a multi-step stress relaxation ageing (SRA) process of aluminium alloy 7050 with a chemical composition of 5.7-6.7 wt% Zn, 1.9-2.6 wt% Mg and 2-2.6 wt% Cu, 0.12 wt % Si, 0.15 wt% Fe, 0.1 wt % Mn. The SRA behaviour has been experimentally examined in detail in (Zheng et al., 2018). A brief review of the test procedure is provided here for completeness.

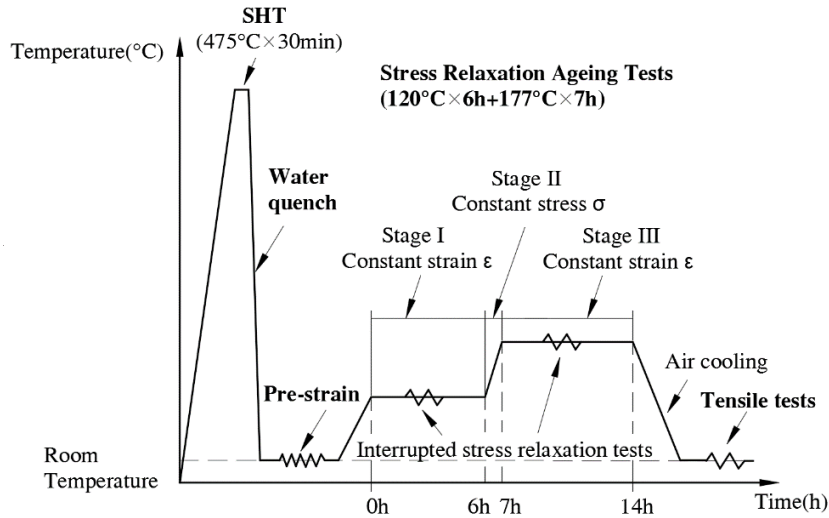## 3.1 Experimental SRA procedure

Figure 1 Schematic illustration of the sample preparation and SRA procedure

In preparation for the SRA tests, all samples were initially solution heat treated (SHT) at 475 °C for 30 minutes and then quenched in warm water (60–70 °C). Subsequently, within 1 hour after quenching, these as-quenched samples were pre-strained to a total strain of 1% and 3%. SRA tests during a multi-step T74 heat treatment process (120 °C × 6 h + 177 °C × 7 h) were carried out on the pre-strained samples. The SRA test procedure is illustrated in Figure 1 and divided into three stages:

Stage I (Constant strain control): Samples were loaded in tension to various initial stresses (i.e. 220 MPa, 270 MPa, 320 MPa, 360 MPa) after the temperature stabilised at 120 °C. The samples were then held at constant strain, enabling the stress relaxation process;

Stage II (Constant stress control): Samples were held at the relaxed stress for 1h during which the temperature was raised from 120 °C to 177 °C.

Stage III (Constant strain control): Samples were again held at constant strain at 177 °C for 7 h, and stress relaxation was monitored.

The yield strength evolution during SRA was determined by conducting room temperature tensile tests on interrupted SRA samples at different times (i.e. 0, 3, 6, 7, 10, 14 h). The detailed experimental procedure and test results can be found in (Zheng et al., 2018). It should be noted that before the onset of SRA (i.e. $t = 0$ h), there was 1h's heating up period from room temperature to 120 °C (detailed temperature curves are given in Figure 4(a)), and hence the precipitation process was already activated. Hence, strictly the evolution of precipitation-related parameters (i.e. $\bar{r}, \bar{f}, \sigma_{ppt}$) commenced prior to the time denoted 0 h in Figure 1.

3.2 TEM tests on typical T74 aged samples

Transmission Electron Microscopy (TEM) tests were conducted on a selection of interrupted pure-aged specimens (i.e. at $t = 6, 8, 14$ h) to examine the evolution of the precipitates during T74 ageing. The temperature employed was the same with that for SRA tests (i.e. 120 °C × 6 h + 177 °C × 7 h). In preparation for TEM, the specimens were firstly cut and ground down to ∼ 150 um, then punched to generate foil discs of diameter 3 mm. These foil discs were finally Twin jetted using a mixture of 275 ml nitric acid and 825 ml methanol at -20 °C to further thinning down to ∼ 40 − 60 nm. The TEM tests were performed using Jeol TEM 2100 Plus electron microscope operating at 200 Kv.

13

The bright field TEM images of the pure aged samples at t = 6, 8 and 14h are presented in Figure 2, together with the T74 ageing temperature profile. From these TEM images, the precipitate evolution during the T74 pure ageing treatment can be observed. After 6h's pure ageing at the 120 $^\circ$ C, Figure 2 (b), finely distributed small precipitates were nucleated. Most of the precipitates have a cigar-like morphology and are ~1-6 nm in length while ~1 nm in width. These precipitates are large in density, however, are too small to provide high dislocation cutting strength, thus making the material remain in the under-aged condition. After raising the temperature to 177 $^\circ$ C and continuously heating to t = 8h, the precipitates gradually grow to around 5-12 nm (i.e. radius: 2.5-6 nm) with a plate shape, as shown in Figure 2 (c). These precipitates are large enough to provide high dislocation cutting strength, while being appropriately small to avoid the dislocation bowing (softening) phenomenon (Polmear, 2005), thus exhibiting high resistance to dislocation motion. The finding is similar to most of the literatures that studied the precipitate evolution of 7xxx serious alloys (Dumont et al., 2003; Liu et al., 2014; Sha and Cerezo, 2004; Stiller et al., 1999; Werenskiold et al., 2000; Zang et al., 2012). With the ageing time continuing to increase, the material will achieve the peak aged state, where all elements are assumed depleted and occupied by the precipitates, and further, coarsen to realise the T74 over-aged states. The coarsening of the precipitates during over-ageing can only be achieved by competitive growth, leading to precipitates with larger sizes as well as smaller density. As expected, the precipitates in the T74 pure aged samples, shown in Figure 2 (d), are larger in size, while smaller in density. The size range is from around 5 nm to 20 nm (i.e. radius: 2.5-10 nm) and most of the precipitates are platelets. Comparing the precipitate size and distributions in Figure 2 (b), (c) and (d), the evolution of the precipitation, including precipitate nucleation (i.e. Figure 2 (b)), growth (Figure 2 (b)→(c)) and coarsening (Figure 2 (c)→(d)), is clearly observed.
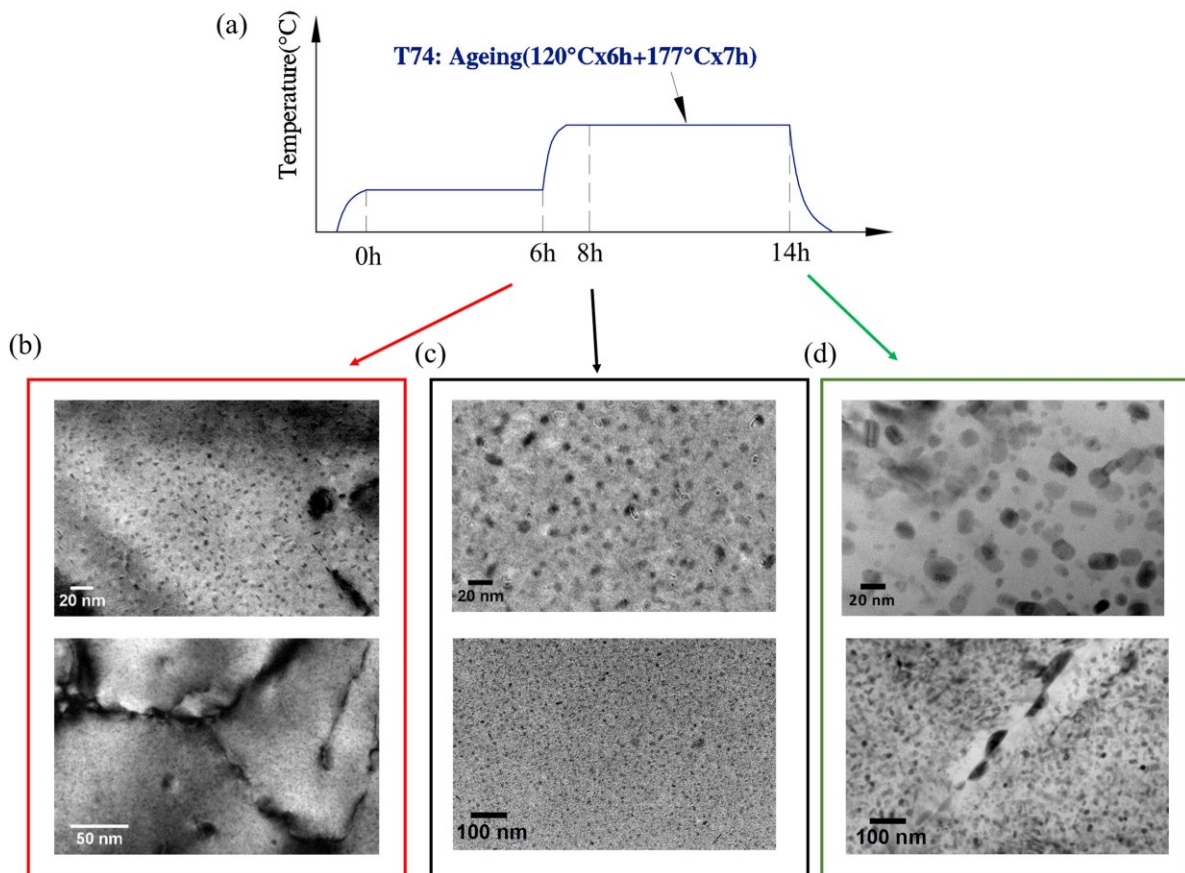

Figure 2 (a) the temperature profile of the T74 ageing treatment. The bright field TEM images of the interrupted aged samples at (b) t= 6, (c) t= 8 and (d) t=14h.

3.3 The evolution of the micro-variables during the T74 ageing treatment
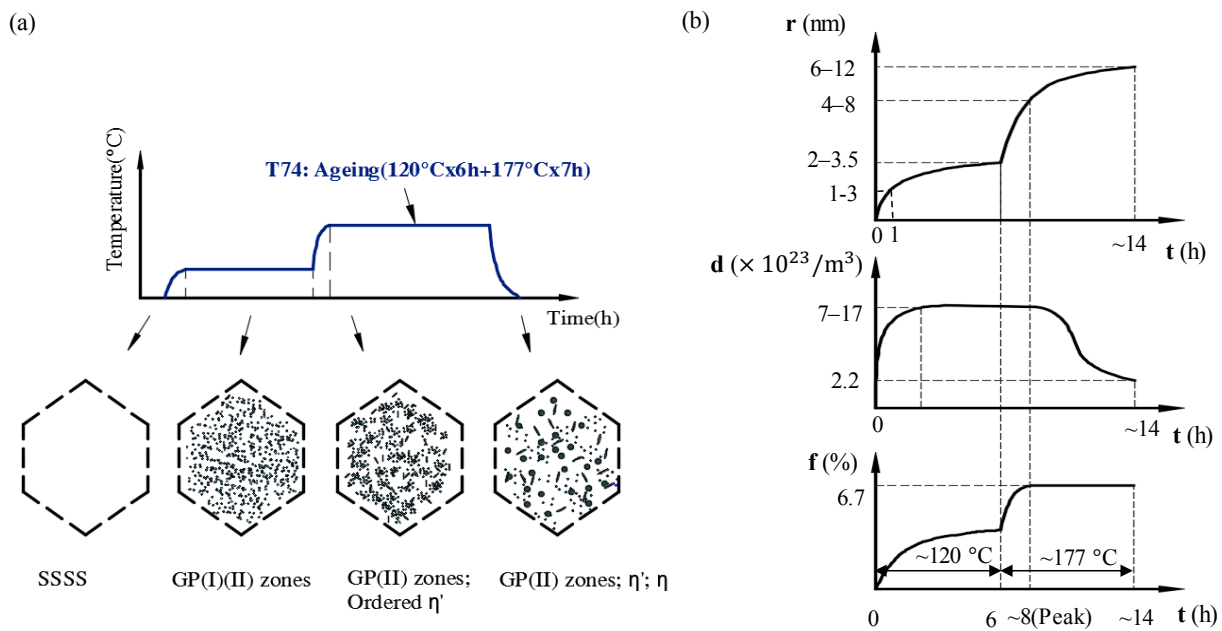

Figure 3 (a) Schematic illustration of age-hardening mechanism and (b) evolutions of precipitate radius (Dumont et al., 2003; Liu et al., 2014; Sha and Cerezo, 2004; Stiller et al., 1999; Werenskiold et al., 2000; Zang et al., 2012), r, density (Sha and Cerezo, 2004; Stiller et al., 1999), d, volume fraction (Han et al., 2011), f, during T74 ageing treatment

A schematic illustration is provided in Figure 3 to facilitate the understanding and calibration of the evolution of the internal variables during the T74 ageing treatment. The original state of the materials is a supersaturated solid solution (SSSS) in preparation for the subsequent ageing treatment (Poole, 1997). It has been accepted that ageing at a low–temperature stage (i.e. 120 °C) results in a relatively high response to hardening due to the nucleation and formation of finely dispersed precipitates (i.e. GP zones and vacancy rich clusters) (Polmear, 2005). These precipitates are relatively small in size (i.e. around $2 - 3.5$ nm (Dumont et al., 2003; Sha and Cerezo, 2004; Werenskiold et al., 2000; Yang et al., 2015)), while extremely high in density (i.e. around $7 - 17 \times 10^{24} m^{-3}$ (Sha and Cerezo, 2004)). The large amount of small shearable precipitates act as obstacles and hinder the dislocation motion, resulting in a relatively high yield strength, as well as high creep resistance. The evolution of the precipitate size, r, density, d, and volume fraction, f, at the low temperature stage are summarised in Figure 3(b). Note that the precipitate density rapidly saturates after exposure to $\sim$ 120 °C (Stiller et al., 1999; Deschamps et al., 1998) and remains constant until the material reaches its peak strength.

A subsequent high-temperature stage efficiently accelerates the precipitation process through bringing higher energy to the pre-existing precipitates, enabling a faster growth of the precipitates. Platelet or cigar-like semi-coherent η', which is believed to be the main strengthening phase, can be rapidly obtained within 1–3 hours of ageing at 177 °C. The rapid increase in the precipitate size from $\sim$2-3.5 nm to $\sim$5 nm (Werenskiold et al., 2000; Yang et al., 2015) is the main reason for the increase in the creep resistance from the under-aged to peak-aged states. The ordered η' continues to grow until the majority of the precipitate transforms into the incoherent η phase and the samples reaching their over-aged T74 states (Polmear, 2005). It is believed that all available elements (e.g. Zn, Mg) in the aluminium matrix are occupied by the precipitates after the samples

15

reach their peak-aged state (Zhan et al., 2011). Thus, η can be formed only by joining η' together leading to an increase in size, a plateau in volume fraction and a decrease in density. The evolutions of the precipitate radius, density and volume fraction at the high temperature stage can be found in Figure 3 (b) with their typical values annotated. These values will be normalised and compared with the predicted $\bar{r}$ from the model in the following section.

3.4 Determination of material constants used for SRA with different initial stresses (Pre-strain = 1%)

The simplest way to fit the strength and stress relaxation curves is to use numerical optimisation methods. These methods, such as the non-linear least squares curve fitting method and genetic algorithm, can give the best fit by trying different sets of material constants to minimise the errors between the predicted and experimental data. However, several problems can occur during fitting. For example, the algorithm optimising to a local minimum or produces material parameters that do not make physical sense. To overcome these difficulties, a combination of manual and computational curve fitting method was employed. All curves, including micro-variables ($\bar{r}$, $\overline{f}$, $\bar{\rho}$), strength evolutions ($\sigma_y, \sigma_{ppt}, \sigma_{solute}, \sigma_{dis}$) and stress relaxation curves (σ), were manually fitted to an initial point for the optimisation process that will result in sensible values. Then, a non-linear least square curve fitting method was employed to further improve the fitting. The detailed procedures are given below:

(i)   Determination of temperature:

According to the T74 temperature profile, the transient temperature evolution, *T*, during Stage II of SRA, increases from the constant value of 393K in Stage I to 450K in Stage III. The temperature change with time at this stage must be described. This transient temperature profile was measured during SRA and may be accurately described using Eqn. (30), as illustrated in Figure 4(a), where the solid line represents the fit to the experimental data. This *T* evolution expression can be input into the model.

$$\dot{T} = 5.5 \times (450 - T) \tag{30}$$

(ii)   Determination of $\bar{R}_{max}$ (Eqn. (5)):

The $\bar{R}_{max}$ evolution was determined using experimental data taken from (Werenskiold et al., 2000). $\bar{R}_{max0}$ and Q_v in Eqn. (5) was obtained by comparing the predicted and experimental results, shown in Figure 4 (b). For clarity, the experimental data plotted in Figure 4 (a) are the average precipitate radius, *r*, normalised by its peak aged radius, r_c, after 24 hours of ageing at different temperatures in (Werenskiold et al., 2000). The results in (Werenskiold et al., 2000) show that *r* increases asymptotically to a saturated value after 24 hours' ageing. Therefore, these saturated values (*r* at 24 h) are regarded as the maximum average precipitate sizes and compared with the predicted $\bar{R}_{max}$.
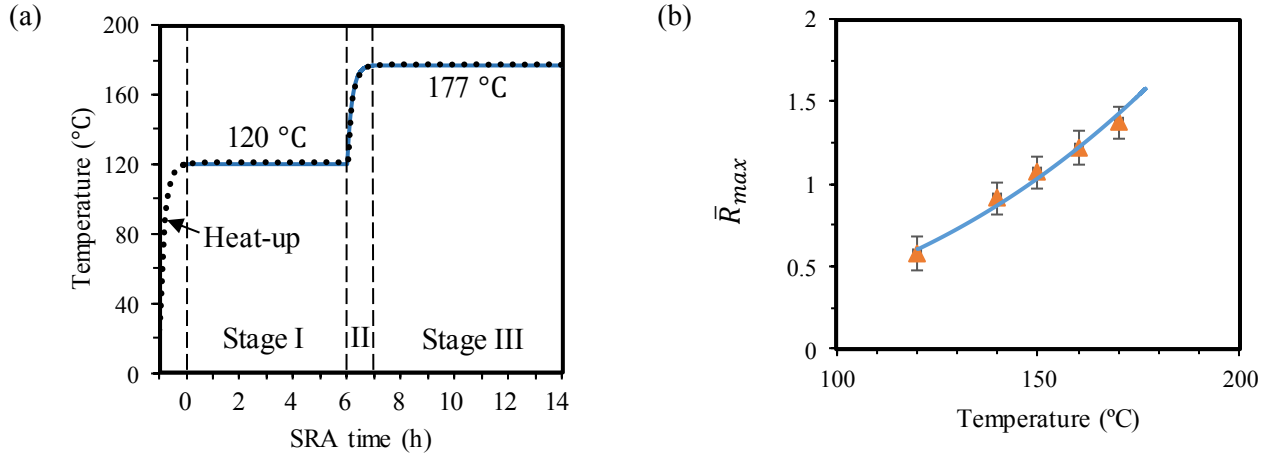
Figure 4 The predicted (solid line) and experimental (dots and symbols) (a) T74 temperature evolution; (b) normalised maximum precipitate radius, $\bar{R}_{max}$, vs Temperature. The experiment data of $\bar{R}_{max}$ is taken from (Werenskiold et al., 2000).

(iii)   Determination of $\bar{r}$ and $\bar{f}$ (Eqns. (4), (7), (10)):

The constants describing $\bar{r}$ and $\bar{f}$ under T74 pure ageing conditions, where $\rho = 0$, were determined by comparing the predicted $\bar{r}$ and $\bar{f}$ evolutions with both the TEM results and the curves shown in Figure 3(b) (Dumont et al., 2003; Liu et al., 2014; Sha and Cerezo, 2004; Stiller et al., 1999; Werenskiold et al., 2000; Zang et al., 2012; Zheng et al., 2018). The experimentally determined radius after 1h's ageing at 120 °C from the literature (Werenskiold et al., 2000) was employed as a good approximation to the initial value of $\bar{r}$ (~0.42) since there is a 1 hour heating up period from room temperature to 120 °C before SRA (i.e. Figure 4 (a)).

(iv)   Determination of $\bar{\rho}$ (Eqns. (12), (13)):

The initial normalised dislocation value, resulting from the 1% pre-strain process, was then introduced into the determined pure-ageing equations. Adjustments were made on $\bar{r}$ and $\bar{f}$ to accommodate the effects of dislocations.

(v)   Determination of $\sigma_y, \sigma_{ppt}, \sigma_{solute}$, and σ_{dis} (Eqns. (14), (20), (23), (24)):

The constants describing the strength evolutions were determined by comparing predicted curves to yield strength evolution data (Zheng et al., 2018).

(vi)   Determination of ε_c and σ (Eqns. (27), (28), (29)):

Finally, the stress relaxation related constants in Eqn. (27) were determined. The stress exponent, $n(1 + \rho)$, was evaluated from a power-law regression fit of the creep strain rate vs stress data. Detailed analysis was presented in (Zheng et al., 2018). The remaining constants were estimated by comparing the predicted and experimental stress relaxation curves, shown in Figure 7.

(vii)   Final determination of material constants:

After obtaining all fitted constants, these constants were used as an initial guess in the optimisation algorithm. In this work, the "lsqnonlin" function in Matlab, which implements the Truss region method, was used (MathWorks, 2017).

The material constants determined through the above procedures are listed in Table 2.

Table 2 Material constants for AA7050 in multi–step SRA

n (-)	m_1 (-)	C_r (h^{-1})	m_2 (-)	C_{ss} (MPa)	B_{ss} (-)	m_3 (-)
1.75	0.18	1100.00	1.00	247.00	0.60	0.67
A_{ds} (MPa)	m_4 (-)	A_r (h^{-1})	a_c (-)	α_1 (-)	m_{r_1} (-)	m_r (-)
95.00	0.77	0.04	1.05 e4	25.32	1.00	2.00
A_f (-)	A_d (-)	m_5 (-)	A_{s_0} (h^{-1})	k_0 (-)	C_{d_0} (h^{-1})	$\bar{R}_{max_0}$ (-)
12.16	37.62	2.58	0.30	4.50 e-4	837.21	1170.00
Q (kJ/mol)	Q_v (kJ/mol)	Q_c (kJ/mol)	σ_0 (MPa)			
23.19	24.67	13.00	1.00			

3.5   Model validation and discussion

The material constants in Table 2 were applied to the constitutive equations proposed above. The T74 multistep stress relaxation ageing (SRA) post 1% pre-strain treatment with different initial stresses was predicted and shown in Figure 5 (micro-variable evolution), Figure 6 (strength evolution) and Figure 7 (stress relaxation).
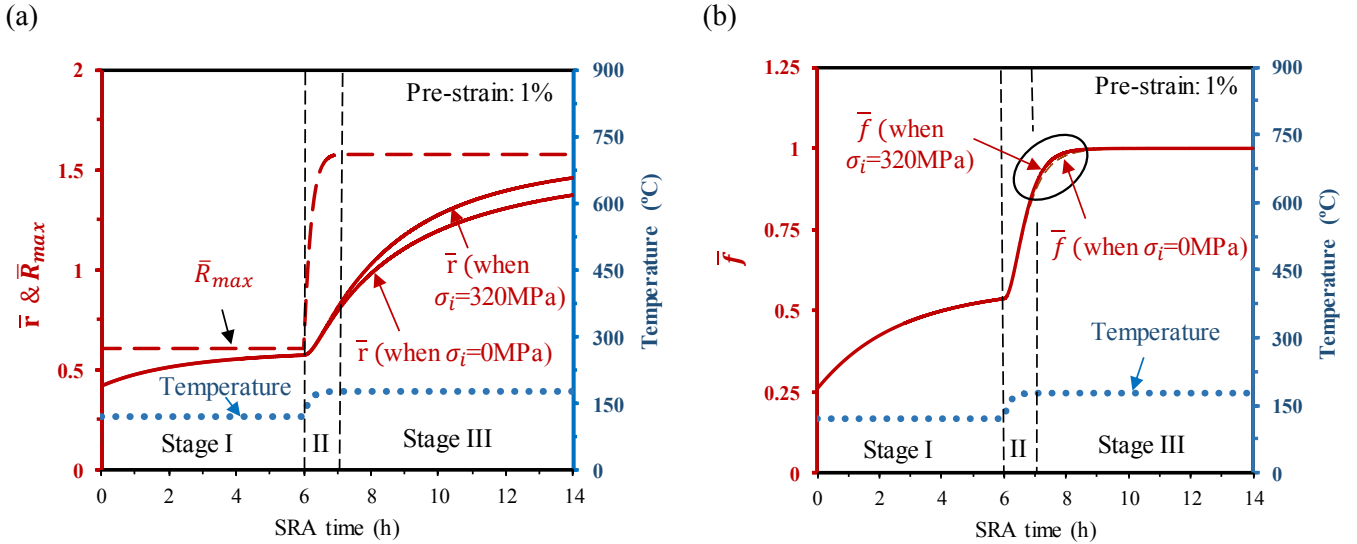
(a)   (b)

Figure 5 The predicted (a) evolution of normalised precipitate radius, $\bar{r}$; (b) evolution of normalised volume fraction, $\bar{f}$, during the stress relaxation ageing process (i.e. $120°C \times 6h + 177°C \times 7h$). Note that the initial stresses (i.e. σ_i) for the stress relaxation is 0 MPa and 320 MPa.

Figure 5(a) shows the predicted evolution of $\bar{r}$ and $\bar{R}_{max}$ during the multi-step SRA for different initial stresses (σ_i). The temperature evolution is also shown as a dotted line. $\bar{R}_{max}$ remains constant at the two isothermal stages, Stage I and III, while it increases with temperature in Stage II. This value limits the

evolution of $\bar{r}$, which increases slowly at Stage I, then increases rapidly at Stage II and III. The observation agrees with the mechanism described in Section 3.2 and 3.3. The evolution of $\bar{r}$ is also affected by the initial stresses (σ_i). Higher σ_i leads to larger creep strains and stress reductions, shown in Figure 7, thus generating more dislocations into the aluminium matrix. These dislocations dynamically promote the precipitation process (Deschamps et al., 1998) resulting in faster nucleation, growth and coarsening of the precipitates. This physical phenomenon was detailed in Figure 5(a), where $\bar{r}$ increases faster in SRA with $\sigma_i = 320$ MPa compared to that with $\sigma_i = 0$ MPa. Note that the influence of σ_i on $\bar{r}$ is negligible during Stage I, and becomes increasingly significant during Stage II and III. This is because negligible creep strains were generated at 120 °C (Figure 7), leading to less dislocation effects on the evolution of $\bar{r}$ at Stage I. To validate the predicted $\bar{r}$ evolution, the average precipitate radius at the peak aged state, r_c, was calculated from the TEM results in our previous work (Zheng et al., 2018) (i.e. r_c=~5 nm). The normalised precipitate radius under different ageing conditions were also calculated using the TEM results (i.e. Figure 2) in this work, which are listed in Table 3. However, the TEM results were only obtained under selected conditions and not sufficient to describe a whole precipitate size evolution, especially the size evolution at Stage I, during SRA. Therefore, the experimental precipitate radius (under T74 pure ageing conditions) were also collected from the literature (Dumont et al., 2003; Han et al., 2011; Liu et al., 2014; Sha and Cerezo, 2004; Stiller et al., 1999; Werenskiold et al., 2000; Zang et al., 2012) and listed together with the TEM data from this study in Table 3 to further validate the predicted $\bar{r}$ trend. Note that all these experimental data are from the TEM results for 7xxx (i.e. Al-Zn-Mg) aluminium alloy, which contains similar chemical composition, and was aged at similar temperature with that of the material used in this study. Thus, the precipitates evolution from literature (i.e. 7xxx aluminium alloy) is expected to be the same with that of AA7050 in this study, where GP zones, η' and η formed sequentially. The precipitate size ranges and evolutions should also be similar to that in this study. To ensure the accuracy of the collected TEM results, firstly, the peak aged precipitate radius, r_c, from (Liu et al., 2014; Werenskiold et al., 2000) is compared with the TEM data in (Zheng et al., 2018), where both of them are ~5 nm. Secondly, the precipitate radius, r, obtained from the literature was also compared with the TEM results in this work, where the range of the precipitates at the same ageing time are basically consistent (Table 3). Thirdly, each selected TEM range were taken from at least two references to ensure reliability. The experimental precipitate radius ranges both from our TEM tests and from the literatures are list in Table 3, and the normalised experimental radius were calculated. As can be seen, the predicted $\bar{r}$ values are both within the range of $\bar{r}_e$ and $\bar{r}_{\text{TEM}}$, suggesting that reasonable predictions of $\bar{r}$ evolution were achieved. The precipitation process had activated before the onset of SRA ($t = 0$ h) during the heating–up period, annotated in Figure 4 (a). Therefore, the initial value of $\bar{r}$ is 0.42 (not 0), as explained above.

Table 3. Experimental (Dumont et al., 2003; Han et al., 2011; Liu et al., 2014; Sha and Cerezo, 2004; Stiller et al., 1999; Werenskiold et al., 2000; Zang et al., 2012) and predicted precipitate radius under T74 pure ageing conditions

Ageing time	0 h (after heating–up)	6 h	8 h	peak	14 h
Experimental radius, r_e, from literatures	1–3 nm (Sha and Cerezo, 2004; Werenskiold et al., 2000; Zang et al., 2012)	2–3.5 nm (Sha and Cerezo, 2004)	-	3.2–8.44 nm (Han et al., 2011; Liu et al., 2014) (Average size: ~4.48-5.00 nm (Liu et al., 2014; Werenskiold et	6–14.1 nm (Han et al., 2011; Stiller et al., 1999)

				al., 2000))	
Normalised experimental radius, $\bar{r}_e = \frac{r_e}{5\,nm}$, from the literatures	0.20–0.60	0.40–0.70		1.00	1.20–2.82
Experimental radius, r_{TEM}, from the TEM	-	1-3 nm	2.5-6 nm	~5.00 nm	2.5-10 nm
Normalised experimental radius, $\bar{r}_{TEM} = \frac{r_{TEM}}{5\,nm}$, from the TEM	-	0.20-0.60	0.50-1.20	1.00	0.50-2.00
Predicted normalised precipitate radius, $\bar{r}$	0.42	0.58	0.98	1.00	1.38

Figure 5(b) shows the predicted normalised volume fraction, $\bar{f}$, evolution during SRA with an initial stress of 0 and 320 MPa. Similar trends were observed compared to that in Figure 5(a), as $\bar{f}$ is strongly affected by the precipitate size (Eqn. (10)), except for that the value of $\bar{f}$ saturated at ~8 h. In addition, $\bar{f}$ saturates faster with higher initial stresses.
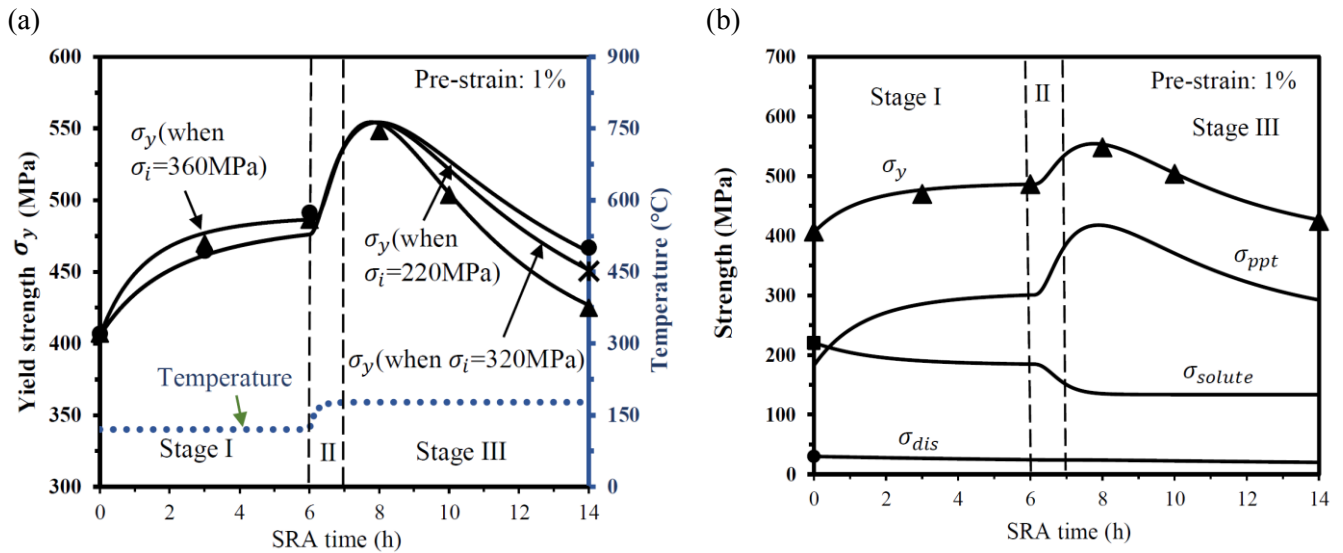

Figure 6 The predicted (solid line) and experimental (symbols) (a) yield strength evolution, σ_y, during the stress relaxation ageing process (i.e. $120°C \times 6h + 177°C \times 7h$) with different initial stresses, σ_i, (b) yield, σ_y, precipitate, σ_{ppt}, solid solute, σ_{solute}, and dislocation, σ_{dis}, strength evolutions in SRA with $\sigma_i = 360MPa$.

The strength vs. time curves are illustrated in Figure 6 together with the experimental data under different initial stresses. Good agreements are achieved, where higher initial stresses facilitate precipitate growth, thus resulting in a faster increase in the yield strength until a peak value and a subsequent decrease. One of the yield strength curves ($\sigma_i = 360 MPa$.) in Figure 6(a) was selected and plotted again in Figure 6 (b) with the evolutions of its strength components ($\sigma_{ppt}, \sigma_{solution}, \sigma_{dis}$). σ_{ppt} varies in the same way as σ_y due to the precipitate evolution, while σ_{solute} varies in the opposite way, due to the solid solute loss in SRA. σ_{dis} decreases slightly with SRA time suggests that dislocation recovery magnitude is larger than the generation magnitude from creep. Though not shown, the alloy's yield strength (measured experimentally) increased from 220 MPa to 250 MPa after pre-straining, and then increased again to 407 MPa after 1 hour's heat-up from room temperature to 120 °C prior to SRA. Therefore, the initial values of the strength contribution from solute strengthening, σ_{solute_i} and dislocation strengthening, σ_{dis_i} ($t = 0$ h in Figure 6 (b)) are set to be 250 MPa and 30 MPa, respectively, while assuming that the solute loss and dislocation static recovery in the heat-up period are negligible. Note that σ_{solute_i} was obtained by conducting uniaxial tensile tests on the quenched sample. Therefore, σ_{solute_i} (i.e. 220 MPa) includes both the solute strength and the quenching induced dislocation strength, if there are any. σ_{dis_i} only accounts for the work hardening induced dislocation strength. During quenching, a small amount of closed-loop dislocations may be formed due to the annealing of the pre-existing vacancies and the plastic flow of the atoms, especially near the triple points of grain boundaries. However, the quantity of the quenching induced dislocations in Al alloy is extremely small compared to that created by the subsequent cold work (Nicholson 1962). Therefore, σ_{solute_i}=220 MPa and σ_{dis_i}=30 MPa can capture the total strength (including solute strength, quenching induced dislocation strength and work hardening induced dislocation strength), except for that the negligible amount of quenching induced dislocations was ignored in σ_{dis_i}. The initial values were plotted in Figure 6(b), σ_{ppt_i} was then calculated using Eqn. (14).

Figure 7 illustrates the predicted and experimental stress relaxation curves. Although slight variations between predicted and measured stress relaxation curves are seen at the beginning of SRA, a generally good agreement was achieved.
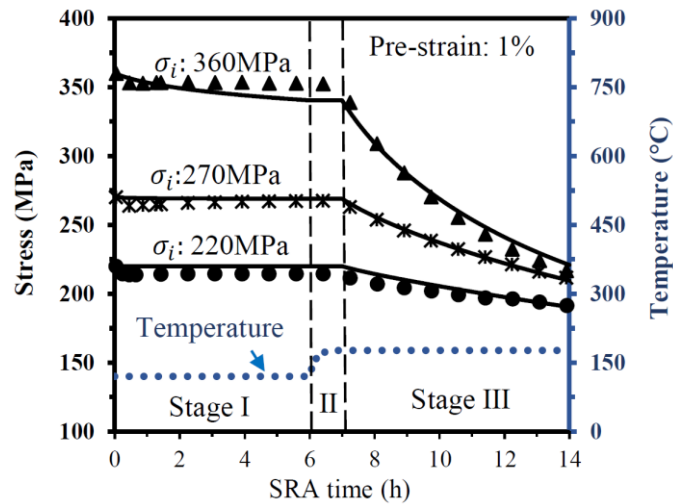

Figure 7 Comparison between predicted (solid line) and experimental (symbols) (Zheng et al., 2018) stress relaxation curves of 7050 Al- alloy with different initial stress levels.

From the results shown in Figure 5, Figure 6 and Figure 7, one can conclude that the set of material constants and constitutive equations can appropriately predict the multi-step SRA behaviour for different

initial stresses. In addition, the microstructure evolutions $(\bar{r}, \bar{f}, \bar{\rho})$ can be reasonably described, where their evolutions show physics based responses to both the temperature and the creep strains in SRA. Pure ageing evolutions can also be described in the model by setting the creep strain rate to zero ($\dot{\varepsilon}_c = 0$). An additional application in using this model to predict the SRA behaviour post different pre-strain levels will be discussed in the next section.

4   Application to different pre-strain conditions

(a)   (b)
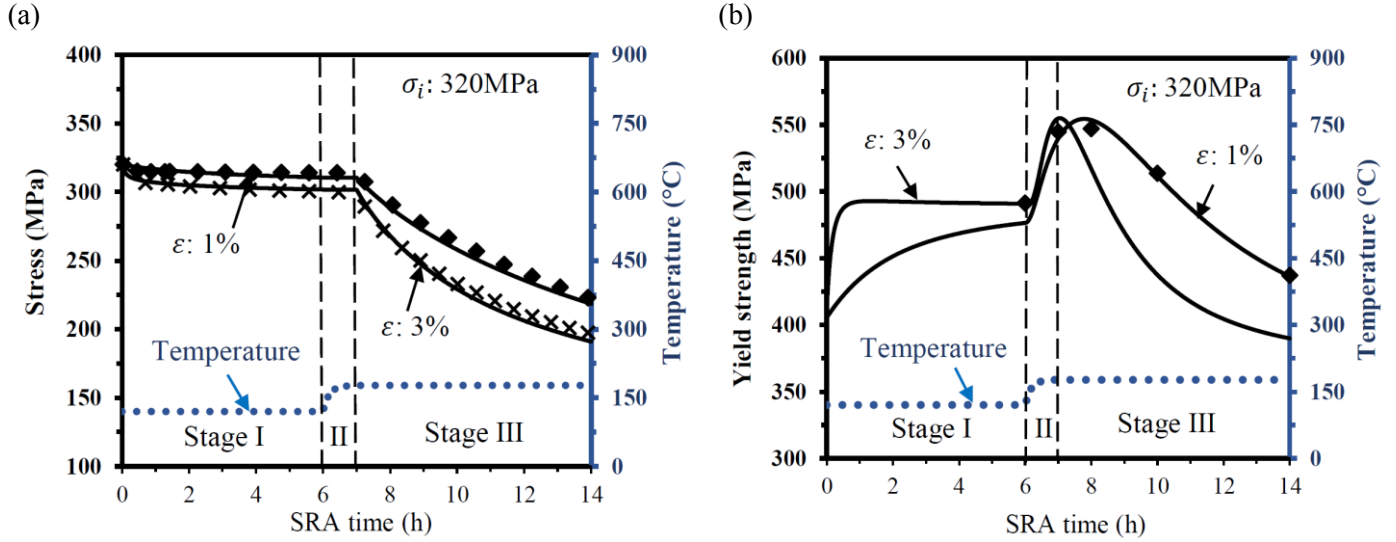

Figure 8 Comparison between the predicted (solid line) and experimental (symbols) (a) stress relaxation and (b) yield strength evolution curves of 7050 Al-alloy during the stress relaxation ageing process (i.e. $120°C \times 6h + 177°C \times 7h$). The initial stress for is 320 MPa, pre-stretch levels prior to SRA are 1% and 3%.

The calibrated models developed were further applied to predict the SRA behaviour post different pre-strain levels with an initial stress of 320 MPa. The effects of pre-strain levels were introduced by calculating the initial normalised dislocation density, $\bar{\rho}_i$, using Eqn. (31), which is an integrated form of Eqn. (12), neglecting the static recovery at room temperature (i.e. $C_d = 0$).

$$\bar{\rho}_i = 1 - exp(-A_d \cdot \varepsilon_{pre}) \tag{31}$$

where ε_{pre} denotes the plastic strain values induced by different pre-strain treatments.

As illustrated in Figure 8, both the predicted stress relaxation and the yield strength curves are in good agreement with the experimental results. Though no experimental data exists, the predicted yield strength of a 3% pre-strained sample (Figure 8(b)) is as expected, where a larger $\bar{\rho}_i$ significantly enhances the ageing response during Stage I (Zheng et al., 2018). The comparison confirms that this model can also give a good prediction of SRA under different pre-strain conditions.

The set of equations can be applied to predict the multi-dimensional stress-strain state using the plastic flow rule, and thus be implemented into commercial FE codes through user-defined subroutines for process modelling (Heinz et al., 2000). It not only can be used to predict the residual stress distribution after ageing but is also capable of predicting the spring-back after the stress-relaxation controlled creep-age-forming (CAF) process. Detailed microstructure and mechanical property evolution in the forming process can also be predicted. This model is currently being used to predict the residual stresses, and mechanical properties in a manufacturing process and findings and results from this work will be published in the near future.

22

5   Conclusions

A set of constitutive equations, based on atomic diffusion and dislocation creep laws, were proposed to predict the stress relaxation ageing (SRA) behaviour of AA 7050. These equations are capable of simulating precipitation response, the simultaneous stress relaxation behaviour and their interactions, by considering the response of strength (yield strength, precipitate strength, solute strength and dislocation strength) and creep to the microstructure evolutions during the SRA process. Three micro-structural internal variables (normalised precipitate radius, volume fraction, dislocation density) were introduced into the equations. Their interactions were quantitatively described by considering the proportions of the bulk diffusion and dislocation core diffusion mechanisms. Temperature effects on these internal variables were also considered, which enables the equations to be applied at different temperatures.

This set of equations was verified by predicting a T74 multi-step SRA behaviour, both with different initial stresses and under different pre-strain conditions. Good agreement, including the stress relaxation and yield strength curves, was obtained between the predicted and experimental results. The progression of precipitation-related variables (i.e. $\bar{r}, \bar{f}$) with time and their response to dislocation evolution were suitably predicted. The validated multi-step SRA constitutive models developed in this work have great potential in practical applications, and can provide valuable guidelines for predicting the residual stress reduction in extra-large aircraft components after the T74 ageing treatment.

Reference

Adzima, F., Balan, T., Manach, P.Y., Bonnet, N., Tabourot, L., 2017. Crystal plasticity and phenomenological approaches for the simulation of deformation behavior in thin copper alloy sheets. International Journal of Plasticity 94, 171-191.

Ahad, F.R., Enakoutsa, K., Solanki, K.N., Bammann, D.J., 2014. Nonlocal modeling in high-velocity impact failure of 6061-T6 aluminum. International Journal of Plasticity 55, 108-132.

Balluffi, R.W., 1970. On measurements of self-diffusion rates along dislocations in F.C.C. Metals. physica status solidi (b) 42, 11-34.

Bardel, D., Fontaine, M., Chaise, T., Perez, M., Nelias, D., Bourlier, F., Garnier, J., 2016. Integrated modelling of a 6061-T6 weld joint: From microstructure to mechanical properties. Acta Materialia 117, 81-90.

Barlat, F., Glazov, M.V., Brem, J.C., Lege, D.J., 2002. A simple model for dislocation behavior, strain and strain rate hardening evolution in deforming aluminum alloys. International Journal of Plasticity 18, 919-939.

Bertin, N., Capolungo, L., Beyerlein, I.J., 2013. Hybrid dislocation dynamics based strain hardening constitutive model. International Journal of Plasticity 49, 119-144.

Brown, A.M., Ashby, M.F., 1980. Correlations for diffusion constants. Acta Metallurgica 28, 1085-1101.

Deschamps, A., Brechet, Y., 1998. Influence of predeformation and agEing of an Al–Zn–Mg alloy—II. Modeling of precipitation kinetics and yield stress. Acta Materialia 47, 293-305.

Deschamps, A., Livet, F., Bréchet, Y., 1998. Influence of predeformation on ageing in an Al–Zn–Mg alloy—I. Microstructure evolution and mechanical properties. Acta Materialia 47, 281-292.

Dumont, D., Deschamps, A., Brechet, Y., 2003. On the relationship between microstructure, strength and toughness in AA7050 aluminum alloy. Materials Science and Engineering: A 356, 326-336.

Esmaeili, S., Lloyd, D.J., Poole, W.J., 2003. A yield strength model for the Al-Mg-Si-Cu alloy AA6111. Acta Materialia 51, 2243-2257.

Farla, R.J.M., Kokkonen, H., Fitz Gerald, J.D., Barnhoorn, A., Faul, U.H., Jackson, I., 2011. Dislocation recovery in fine-grained polycrystalline olivine. Physics and Chemistry of Minerals 38, 363-377.

Frost, H.J., Ashby, M.F., 1973. A second report on deformation mechanism maps.

Frost, H.J., Ashby, M.F., 1982. Deformation-mechanism maps: the plasticity and creep of metals and ceramics. Pergamon Press, Oxford [Oxfordshire]; New York.

Gu, R., Ngan, A.H.W., 2014. Size-dependent creep of duralumin micro-pillars at room temperature. International Journal of Plasticity 55, 219-231.

Haddadi, H., Bouvier, S., Banu, M., Maier, C., Teodosiu, C., 2006. Towards an accurate description of the anisotropic behaviour of sheet metals under large plastic deformations: Modelling, numerical analysis and identification. International Journal of Plasticity 22, 2226-2271.

Han, N., Zhang, X., Liu, S., Ke, B., Xin, X., 2011. Effects of pre-stretching and ageing on the strength and fracture toughness of aluminum alloy 7050. Materials Science and Engineering: A 528, 3714-3721.

Heinz, A., Haszler, A., Keidel, C., Moldenhauer, S., Benedictus, R., Miller, W.S., 2000. Recent development in aluminium alloys for aerospace applications. Materials Science and Engineering: A 280, 102-107.

Ho, K.C., Lin, J., Dean, T.A., 2004. Modelling of springback in creep forming thick aluminum sheets. International Journal of Plasticity 20, 733-751.

Kabirian, F., Khan, A.S., Pandey, A., 2014. Negative to positive strain rate sensitivity in 5xxx series aluminum alloys: Experiment and constitutive modeling. International Journal of Plasticity 55, 232-246.

Kampmann, R., Wagner, R., 1984. kinetics of precipitation in metastable binary alloys -theory and application to Cu-1.9 at % Ti and Ni-14 at % Al Decomposition of Alloys: The Early Stages. Pergamon, pp. 91-103.

Khan, A.S., Liu, J., 2016. A deformation mechanism based crystal plasticity model of ultrafine-grained/nanocrystalline FCC polycrystals. International Journal of Plasticity 86, 56-69.

Kocks, U.F., Argon, A.S., Ashby, M.F., 1975. Models for macroscopic slip. Prog. Mater Sci. 19, 68-93.

Kocks, U.F., 1976. Laws for Work-Hardening and Low-Temperature Creep. Journal of Engineering Materials and Technology 98, 76-85.

Krempl, E., 2001. Relaxation behavior and modeling. International Journal of Plasticity 17, 1419-1436.

Lam, A.C.L., Shi, Z., Lin, J., Huang, X., 2015. Influences of residual stresses and initial distortion on springback prediction of 7B04-T651 aluminium plates in creep-age forming. International Journal of Mechanical Sciences 103, 115-126.

Leyson, G.P.M., Curtin, W.A., Hector Jr, L.G., Woodward, C.F., 2010. Quantitative prediction of solute strengthening in aluminium alloys. Nature Materials 9, 750.

Li, H., Lin, J., Dean, T.A., Wen, S.W., Bannister, A.C., 2009. Modelling mechanical property recovery of a linepipe steel in annealing process. International Journal of Plasticity 25, 1049-1065.

Li, Y., Shi, Z., Lin, J., Yang, Y.-L., Rong, Q., Huang, B.-M., Chung, T.-F., Tsao, C.-S., Yang, J.-R., Balint, D.S., 2017. A unified constitutive model for asymmetric tension and compression creep-ageing behaviour of naturally aged Al-Cu-Li alloy. International Journal of Plasticity 89, 130-149.

Lin, J., Ho, K.C., Dean, T.A., 2006. An integrated process for modelling of precipitation hardening and springback in creep age-forming. International Journal of Machine Tools and Manufacture 46, 1266-1270.

Lin, Y.C., Xia, Y.-C., Chen, M.-S., Jiang, Y.-Q., Li, L.-T., 2013. Modeling the creep behavior of 2024-T3 Al alloy. Computational Materials Science 67, 243-248.

Liu, G., Zhang, G.J., Ding, X.D., Sun, J., Chen, K.H., 2003. Modeling the strengthening response to aging process of heat-treatable aluminum alloys containing plate/disc- or rod/needle-shaped precipitates. Materials Science and Engineering: A 344, 113-124.

Liu, Y., Jiang, D., Li, B., Ying, T., Hu, J., 2014. Heating aging behavior of Al–8.35Zn–2.5Mg–2.25Cu alloy. Materials & Design 60, 116-124.

MathWorks, 2017. MATLAB Non-linear least-squares solver.

Mukherjee, A.K., Bird, J.E., Dorn, J.E., 1968. Experimental correlations for high-temperature creep. California Univ., Berkeley. Lawrence Radiation Lab., p. Medium: X; Size: Pages: 84.

Myhr, O.R., Grong, Ø., 2000. Modelling of non-isothermal transformations in alloys containing a particle distribution. Acta Materialia 48, 1605-1615.

Myhr, O.R., Grong, Ø., Fjær, H.G., Marioara, C.D., 2004. Modelling of the microstructure and strength evolution in Al–Mg–Si alloys during multistage thermal processing. Acta Materialia 52, 4997-5008.

R.B. Nicholson. Quenching defects in solid solutions and their effect on precipitation. J. Phys. Radium, 1962, 23 (10), 824-827.

Nicolas, M., Deschamps, A., 2003. Characterisation and modelling of precipitate evolution in an Al–Zn–Mg alloy during non-isothermal heat treatments. Acta Materialia 51, 6077-6094.

Pan, R., Shi, Z., Davies, C.M., Li, C., Kaye, M., Lin, J., 2016. An integrated model to predict residual stress reduction by multiple cold forging operations in extra-large AA7050 T-section panels. Journal of Engineering Manufacture.

Polmear, I.J., 2005. 3 - Wrought aluminium alloys, in: Polmear, I.J. (Ed.), Light Alloys (Fourth Edition). Butterworth-Heinemann, Oxford, pp. 97-204.

Poole, W.J.S., H R; Castillo, T., 1997. Process model for two step age hardening of 7475 aluminium alloy. Materials Science and Technology 13, 897-904.

Poole, W.J., Sæter, J.A., Skjervold, S., Waterloo, G., 2000. A model for predicting the effect of deformation after solution treatment on the subsequent artificial aging behavior of AA7030 and AA7108 alloys. Metall and Mat Trans A 31, 2327-2338.

Robinson, J.S., Tanner, D.A., van Petegem, S., Evans, A., 2012. Influence of quenching and aging on residual stress in Al–Zn–Mg–Cu alloy 7449. Materials Science and Technology 28, 420-430.

Robinson, S.L., Sherby, O.D., 1969. Mechanical behavior of polycrystalline tungsten at elevated temperature. Acta Metallurgica 17, 109-125.

Sha, G., Cerezo, A., 2004. Early-stage precipitation in Al–Zn–Mg–Cu alloy (7050). Acta Materialia 52, 4503-4516.

Shercliff, H.R., Ashby, M.F., 1990. A process model for age hardening of aluminium alloys—I. The model. Acta Metallurgica et Materialia 38, 1789-1802.

Shi, B., Peng, Y., Yang, C., Pan, F., Cheng, R., Peng, Q., 2017. Loading path dependent distortional hardening of Mg alloys: Experimental investigation and constitutive modeling. International Journal of Plasticity 90, 76-95.

Somekawa, H., Hirai, K., Watanabe, H., Takigawa, Y., Higashi, K., 2005. Dislocation creep behavior in Mg–Al–Zn alloys. Materials Science and Engineering: A 407, 53-61.

Stiller, K., Warren, P.J., Hansen, V., Angenete, J., Gjønnes, J., 1999. Investigation of precipitation in an Al–Zn–Mg alloy after two-step ageing treatment at 100° and 150°C. Materials Science and Engineering: A 270, 55-63.

Taylor, G.I., 1934. The Mechanism of Plastic Deformation of Crystals. Part I.- Theoretical. Proc. R. Soc. London. Ser. A, Contain. Pap. a Math. Phys. Character 145, 362–387.

Wang, J.F., Wagoner, R.H., Carden, W.D., Matlock, D.K., Barlat, F., 2004. Creep and anelasticity in the springback of aluminum. International Journal of Plasticity 20, 2209-2232.

Werenskiold, J.C., A, Bréchet, Y., 2000. Characterization and modeling of precipitation kinetics in an Al–Zn–Mg alloy. Materials Science and Engineering: A 293, 267-274.

Yan, S., Yang, H., Li, H., Yao, X., 2016. A unified model for coupling constitutive behavior and micro-defects evolution of aluminum alloys under high-strain-rate deformation. International Journal of Plasticity 85, 203-229.

Yang, W.C., Ji, S.X., Zhang, Q., Wang, M.P., 2015. Investigation of mechanical and corrosion properties of an Al-Zn-Mg-Cu alloy under various ageing conditions and interface analysis of eta ' precipitate. Materials & Design 85, 752-761.

Yoshida, F., 2000. A constitutive model of cyclic plasticity. International Journal of Plasticity 16, 359-380.

Zang, J.-x., Zhang, K., Dai, S.-l., 2012. Precipitation behavior and properties of a new high strength Al-Zn-Mg-Cu alloy. Transactions of Nonferrous Metals Society of China 22, 2638-2644.

Zhan, L.H., Lin, J., Dean, T.A., Huang, M.H., 2011. Experimental studies and constitutive modelling of the hardening of aluminium alloy 7055 under creep age forming conditions. International Journal of Mechanical Sciences 53, 595-605.

Zhang, Q., Zhang, W., Liu, Y., 2015. Evaluation and mathematical modeling of asymmetric tensile and compressive creep in aluminum alloy ZL109. Materials Science and Engineering: A 628, 340-349.

Zheng, J.-H., Pan, P., Li, C., Zhang, W., Lin, J., Davies, C.M., 2018. Experimental investigation of multi-step stress-relaxation-ageing of 7050 aluminium alloy for different pre-strained conditions. Materials Science and Engineering: A 710, 111-120.